

# Non-thermal emissions from outer magnetospheric accelerators of middle-aged pulsars

J. Takata<sup>1\*</sup> and H.-K. Chang<sup>2,3</sup>

<sup>1</sup>*Institute of Astronomy and Astrophysics, and Theoretical Institute for Advanced Research in Astrophysics, Academia Sinica; and National Tsing Hua University, Hsinchu, Taiwan*

<sup>2</sup>*Department of Physics, National Tsing Hua University, Hsinchu, Taiwan*

<sup>3</sup>*Institute of Astronomy, National Tsing Hua University, Hsinchu, Taiwan*

## ABSTRACT

We discuss  $\gamma$ -ray emissions from the outer gap accelerators of middle-aged pulsars for part of the series of our studies. A two-dimensional electrodynamic model is used to solve the distribution of accelerating electric fields with electron and positron pair creation and radiation processes in the magnetic meridional plane. We compute the curvature radiation and the synchrotron radiation by solving the evolution of the Lorentz factor and the pitch angle. The calculated spectra are compared with observed phase-averaged spectra. We also use a three-dimensional geometrical model to discuss the pulse profiles. We argue that the outer gap of middle-aged pulsars occupies the whole region between the last-open field lines and the critical magnetic field lines, which are perpendicular to the rotational axis at the light cylinder. We assume that there is no outer gap accelerator inside the light cylinder between the rotational axis and the critical magnetic field lines. For the Geminga pulsar, we demonstrate that the outward curvature radiation dominates in the spectrum above 10 MeV, while the inward synchrotron radiation dominates below 10 MeV. We find that the computed spectrum is consistent with the observations in X-ray through  $\gamma$ -ray bands. With the pulse morphology of the  $\gamma$ -ray emissions, we argue that the inclination angle and the viewing angle for the Geminga pulsar are  $\alpha \sim 50^\circ$  and  $\xi \sim 90^\circ$ , respectively. We also apply our method to another four middle-aged radio pulsars, whose spin-down power and distance from the Earth expect the possibility of detection of  $\gamma$ -ray emissions from those pulsars by Fermi telescope. Applying the inclination angle and the viewing angle inferred from radio polarization characteristics, the visibility of the  $\gamma$ -ray emissions from the outer gap is discussed. We show that

$\gamma$ -ray emissions from PSRs B0355+54, B1449-64 and B1929+10 will probably be detectable by Fermi telescope. For PSR B0740-28, on the other hand,  $\gamma$ -ray emissions will not be detected because the  $\gamma$ -ray beam from the outer gap will be oriented in a different direction from the viewing angle.

**Key words:** pulsars: middle-aged pulsars– radiation mechanisms:non-thermal

## 1 INTRODUCTION

The Energetic Gamma-ray Experiment Telescope (EGRET) aboard the *Compton Gamma-ray observatory* detected the gamma-ray emissions from six pulsars (Thompson 2004), five of which show pulsed radio emissions. The sixth, Geminga pulsar, has known as a radio quiet  $\gamma$ -ray pulsar or with very weak radio emissions (Vats et al. 1999). Because of the observed high brightness temperature of radio emissions from pulsars, the radio radiation is a coherent mechanism. On the other hand, the emission mechanisms in optical through  $\gamma$ -ray bands are non-coherent and non-thermal processes, which have been discussed with the polar cap model, the slot gap model and the outer gap model in the literature.

The polar cap accelerator has been considered as the origin of radio emission from pulsars (Ruderman & Sutherland 1975). The configuration of the dipole magnetic field in inner magnetosphere region provides a natural explanation of position-angle curve of polarization of the radio pulse. For  $\gamma$ -ray emissions, however, the polar cap model has to invoke both a small inclination angle and a small viewing angle measured from the rotational axis to reproduce the observed wide separation of the two peaks appeared in the pulse profiles (Daugherty & Harding 1996).

The slot gap model (Arons 1983) is an extension of the polar cap model. The possibility of a high-altitude extension of the accelerator near the last-open field lines was proposed. The recent slot gap model explains the spectrum in optical to  $\gamma$ -ray bands for the Crab pulsar (Muslimov & Harding 2003, 2004; Harding et al. 2008) and the pulse profiles in  $\gamma$ -ray bands for the Vela pulsar (Dyks & Rudak 2003).

The outer gap accelerator model assumes a strong acceleration between the null charge surface of the Goldreich-Julian charge density and the light cylinder (Cheng, Ho & Ruderman 1986a, b). The Goldreich-Julian charge density is described by  $\rho_{GJ} \sim -\Omega B_z/2\pi c$  with  $\Omega$  being the rotation frequency,  $B_z$  the magnetic field component projected to the rotation

axis, and  $c$  the speed of light. The recent studies of the outer gap model also explain the spectra and pulse profiles measured by EGRET (Hirotani 2007; Tang et al. 2008; Takata et al. 2008). Although numerous efforts have been done to discriminate emission models with  $\gamma$ -ray data, the origin of the non-thermal emission remains inconclusive.

In addition to the  $\gamma$ -ray data of EGRET, emission properties in lower energy bands have also been provided. For example, Harding et al. (2002) found that the pulse profile of the Vela pulsar in RXTE bands shows four or five peaks in a single period instead of the double peak structure measured by EGRET. The detail polarization features of optical pulsed emissions from the Crab pulsar have been measured by Kanbach et al (2005). INTEGRAL also measured the polarization of the  $\gamma$ -ray emissions from the Crab pulsar for the first time (Dean et al. 2008). In the future, furthermore, the polarization of X-ray and soft  $\gamma$ -ray emissions from the Crab pulsar will probably be able to be measured by ongoing projects such as PoGo (Kataoka et al. 2005) and the Nuclear Compton Telescope (Chang et al. 2007). Both the *Astro -rivelatore Gamma a Immagini LEggero* (AGILE) and recently launched *Fermi Gamma-Ray Space Telescope* (Fermi, hereafter) will measure more detail features of the phase-resolved spectra and the pulse profiles in 1 MeV through 100 GeV bands. In particular, Fermi telescope is expected to measure pulsed  $\gamma$ -ray emissions from both many radio pulsars and from unidentified EGRET sources. A comprehensive theoretical study with observations in multi-wavelength bands is desired and will be important to discriminate emission models.

Takata et al. (2007) and Takata & Chang (2007) discussed non-thermal emissions from the young pulsars, PSRs B0531+21 (Crab) and B0540-69, with the outer gap model. In Takata et al. (2007), they demonstrated that the outer gap model can explain observed polarization properties of the optical pulsed emissions from the Crab pulsar. Takata & Chang (2007) extended their calculation of the polarization to higher energy band and predicted the results of future observations. Also, they produced observed phase-resolved spectra in optical through  $\gamma$ -ray bands for the Crab pulsar. They predicted that  $\gamma$ -ray flux on the Earth from PSR B0540-69 is about  $10^{-12}$  erg/cm<sup>2</sup>s, which may be a target for Fermi observation.

Takata et al. (2008) discussed the emission process in optical through  $\gamma$ -ray bands for the Vela-like young pulsars. Solving the electrodynamics of the outer gap, they first pointed out that inward emission by ingoing particles is an important component below 10 MeV bands, while only outward emission contributes to the spectrum above 10 MeV as the traditional outer gap model has assumed. They produced the observed multi-peak structure of the pulse

profile in X-ray bands of the Vela pulsar with the inward and the outward emissions. They predicted that the pulse profile at 1-10 MeV has four peaks in a single period, which can be checked in future observations.

We had studied the non-thermal emissions from the Crab-like and the Vela-like pulsars. In this paper, therefore, we discuss the non-thermal emissions from the outer gap of the middle-aged pulsars for part of the series of our studies. Using a two-dimensional electrodynamic model, we will solve the accelerating electric field with electron and positron pair creation and radiation processes (section 3). We will also discuss the X-ray and  $\gamma$ -ray pulse profiles using a three-dimensional geometrical model (section 4). We apply the outer gap model to the Geminga pulsar (section 5.1). The calculated spectrum will be compared with the observed phase-averaged spectrum in X-ray through  $\gamma$ -ray bands. (section 5.1.2). We discuss the inclination angle, which is angle between the rotational axis and the magnetic axis, and the viewing angle with the observed properties of the  $\gamma$ -ray pulse profile for the Geminga pulsar. (section 5.1.3). Also by assuming that the radio beam from the Geminga pulsar is oriented in a different direction from the line of sight, we will further constrain the magnetic inclination angle (section 5.2).

We will also apply the model to another middle-aged radio pulsars (section 5.3), whose timing properties are similar to the Geminga pulsar. We will show candidates for detections by Fermi telescope. With its high sensitivity, Fermi telescope will also be able to identify  $\gamma$ -ray quiet radio pulsars, although their  $\gamma$ -ray emissions should be detectable in the sense of magnitude of the spin-down luminosity and its distance. With the present outer gap study, we will argue that PSR B0740-28 is a candidate of the  $\gamma$ -ray quiet pulsars due to misalignment of the directions of the  $\gamma$ -ray beam and the line of sight.

## 2 MAGNETOSPHERES OF MIDDLE-AGED PULSARS

Figure 1 shows a schematic picture of the magnetosphere model for middle-aged pulsars. In general, we expect that the outer gap can arise between the last-open field lines and the magnetic field lines (so called critical field lines, hereafter) on which the Goldreich-Julian charge density vanishes at the light cylinder. Between the rotational axis and the critical field lines, the null charge surface is located beyond the light cylinder so that the Goldreich-Julian charge density does not change its sign all the way from the stellar surface to the

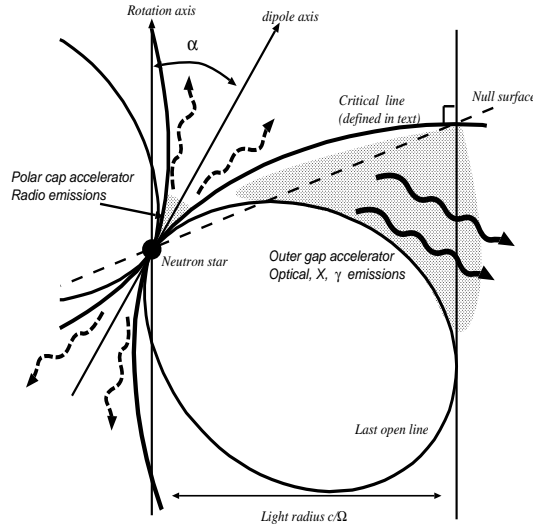


**Figure 1.** Schematic figure of the magnetosphere of middle-aged pulsars. The outer gap (filled region) occupies region between the last-open field line and the critical field line. The radio wave originates from the inner region of the magnetosphere. The optical to  $\gamma$ -ray photons are from the outer gap region. The critical field line (thick solid line) is defined by the magnetic field line on which the Goldreich-Julian density vanishes at the light cylinder.

light cylinder. Therefore, we expect that there is no outer gap in the region between the rotational axis and the critical field lines.

For a static dipole field, the polar angle of the critical field line on the stellar surface in the magnetic meridional plane is

$$\theta_c = \alpha + \sin^{-1} \left[ \sin(\theta_n - \alpha) \left( \frac{R_*}{R_{lc}} \sin \theta_n \right)^{1/2} \right], \quad (1)$$

where  $\alpha$  is the magnetic inclination angle,  $R_*$  is the stellar radius,  $R_{lc} = c/\Omega$  is the light radius, and  $\theta_n$  is the angle of the null charge surface of the Goldreich-Julian density;

$$\theta_n = \tan^{-1} \left( \frac{3 \tan \alpha + \sqrt{8 + 9 \tan^2 \alpha}}{2} \right). \quad (2)$$

We define the trans-field thickness of the maximally extending gap in the magnetic meridional plane with  $\delta\theta_{max} = \theta_{pc} - \theta_c$ , where  $\theta_{pc}$  is the polar cap angle. For the static dipole field, the polar cap angle is expressed by

$$\theta_{pc,0} = \alpha + \sin^{-1} \left[ \sin(\theta_{lc} - \alpha) \left( \frac{R_*}{R_{lc}} \sin \theta_{lc} \right)^{1/2} \right], \quad (3)$$

where

$$\theta_{lc} = \tan^{-1} \left( \frac{-3 - \sqrt{9 + 8 \tan^2 \alpha}}{4 \tan \alpha} \right).$$

For the middle-aged pulsars, we can expect that the thickness of the outer gap becomes to be comparable with the maximum thickness  $\delta\theta_{max}$  as follows. The potential drop on the stellar surface between the critical magnetic field line and the polar cap rim is

$$V_a \sim 1.3 \times 10^{13} P^{-3/2} \dot{P}_{-15}^{1/2} (1 - \sin^3 \theta_n^3) \text{ Volt}, \quad (4)$$

which becomes  $V_a \sim 1.7 \times 10^{14}$  Volt for the Geminga pulsar.

We can show that almost whole potential drop  $V_a$  is required to explain the GeV emissions from the Geminga pulsar. For the Geminga pulsar, a spectral cut off around 2 GeV was measured (Fierro et al. 1998). We estimate whole potential drop in the gap,  $V_{gap}$ , from the cut off energy. We assume that  $\gamma$ -ray photons are emitted via the curvature radiation, and that the particles that emit the cut off photons are accelerated by the whole potential drop along the magnetic field lines in the gap. The typical strength of the accelerating electric field is estimated from  $E_{||} \sim V_{gap}/R_{lc}$ . We assume the force balance between the acceleration and the radiation back reaction force to calculate a typical Lorentz factor of the accelerated particles;  $\Gamma \sim (3R_c^2 E_{||}/2e)^{1/4} \sim (3R_c^2 V_{gap}/2eR_{lc})^{1/4}$ , where  $R_c$  is the curvature radius of the magnetic field line. Using the typical energy of the curvature photons  $E_c \sim 3hc\Gamma^3/4\pi R_c$ , the estimated potential drop in the outer gap is

$$V_{gap} \sim 2.8 \times 10^{14} \left( \frac{E_c}{2 \text{ GeV}} \right)^{4/3} \left( \frac{\Omega}{26.5 \text{ s}^{-1}} \right)^{-1/3} \text{ Volt} \quad (5)$$

where we used  $R_c = R_{lc}$ . We find that the estimated magnitude of the potential drop is comparable with the available potential drop defined by equation of (4) for the Geminga pulsar. The observed  $\gamma$ -ray emissions from the Geminga pulsar imply that most of the region between the last-open field lines and the critical field lines will be occupied by the outer gap for the middle-aged pulsars.

For younger pulsars, the outer gap accelerator occupies about 10 % of the whole region between the last-open field lines and the critical field lines. For example, the available potential drop defined by equation of (4) for the Vela pulsar becomes  $V_a \sim 2.5 \times 10^{15}$  Volt. The observed cut off energy around 3 GeV indicates the potential drop in the gap is about  $V_{gap} \sim 10^{14}$  Volt. Therefore, only about 10 % of the available potential drop is required to explain the  $\gamma$ -ray emissions from the Vela pulsar.

From the dynamic point of view, we can also argue that the outer gap of the middle-aged pulsars occupies most of the region between the last-open field line and the critical field line. The  $\gamma$ -rays emitted by the accelerated particles may convert into electron and positron pairs by the pair creation process with a soft X-ray field from the stellar surface. If typical energy of the curvature photons have an energy such that the pair creation condition  $E_\gamma E_X \geq (m_e c^2)^2$  is satisfied, the outer gap can not develop further due to screening effects of the pairs. In such a case, the position of the upper boundary of the gap is determined

by the pair creation condition. For the Geminga pulsar, however, the pair creation in the outer magnetosphere is not efficient. The temperature of the stellar surface is about  $T_s \sim 0.5$  MK (Kargaltsev et al. 2005), so the threshold energy of the  $\gamma$ -rays for the pair creation is  $E_\gamma \sim (m_e c^2)^2 / kT_s \sim 6$  GeV, where  $k$  is the Boltzmann constant. From equation of (5), the potential drop of  $V_{gap} \sim 10^{15}$  Volt in the gap is required to accelerate the particles to emit 6 GeV photons. However it will be impossible to accelerate the particles because the available potential drop in the outer gap  $V_a \sim 2 \times 10^{14}$  Volt estimated from equation of (4) is smaller than the required potential drop for the pair creation. The particles can not be accelerated in the outer gap to emit 6 GeV photons with the curvature radiation process. Therefore, we expect that the outer gap of the middle-aged pulsars can develop to occupy the region between the last-open field lines and the critical field lines. As we said in the first paragraph in this section, we do not expect that the outer gap accelerator arises beyond the critical field lines, because the Goldreich-Julian charge density does not change its sign all the way from the stellar surface to the light cylinder

We assume that the radio emission originates from the polar cap accelerator, while the emissions in optical through  $\gamma$ -ray bands originate from the outer gap accelerator. Electrodynamically speaking, because of the different flow directions of the electric currents in the polar cap and in the outer gap, the current conservation forces that both acceleration regions do not exit on the same magnetic field lines. In this paper, we anticipate that the outer gap accelerator is extending from the last-open field line to the critical field lines, and the polar cap accelerator extends in a region between the critical field lines and the rotational axis. This assumption will be rejected if the radio emissions take place on the last-open field line. In fact, there are no observational evidences. For example, the phenomenological study with the polarization characteristics for the radio emissions (Dyks et al. 2004) indicates that the outer rim of the radio beam is emitted on the magnetic fields located well above the last-open field lines.

### **3 TWO-DIMENSIONAL ELECTRODYNAMIC OUTER GAP MODEL**

In this section, we briefly summarize our method of the electrodynamic study of the outer gap model. A more detail description of our model can be found in the previous paper (Takata et al. 2004). We solve the accelerating electric field with the radiation and the pair creation processes in the magnetic meridional plane, which includes the rotation axis and

the magnetic axis. In the electrodynamic study, we use a static dipole field to solve the structure of the outer gap. We consider a magnetized rotator in which an inclination angle  $\alpha$  between the rotational axis and magnetic axis is smaller than  $90^\circ$ .

### 3.1 Electrodynamics

The stationary electric potential,  $\Phi_{nco}$ , for the accelerating field in the observer frame is obtained from (Shibata 1995; Mestel 1999)

$$\Delta\Phi_{nco}(\mathbf{r}) = -4\pi[\rho(\mathbf{r}) - \rho_{GJ}(\mathbf{r})], \quad (6)$$

where  $\rho(\mathbf{r})$  is the space charge density, and  $\rho_{GJ}(\mathbf{r})$  is the Goldreich-Julian charge density, for which we use  $\rho_{GJ} = -\Omega B_z/2\pi c$ .

For the steady state, the continuity equations of the particles are written as

$$\mathbf{B} \cdot \nabla \left( \frac{v_{\parallel} N_{\pm}(\mathbf{r})}{B} \right) = \pm S(\mathbf{r}), \quad (7)$$

where  $v_{\parallel} \sim c$  is the velocity along the field line,  $S(\mathbf{r})$  is the source term due to the pair creation process, and  $N_+$  and  $N_-$  denote the number density of the outgoing (positrons) and ingoing (electrons) particles, respectively. In the outer magnetosphere,  $\gamma + X \rightarrow e^+ + e^-$  pair creation process contributes to the source term  $S(\mathbf{r})$ . We simulate the pair creation process with a Monte Carlo method, which is explicitly described in Takata et al. (2004, 2006).

To solve the Poisson equation (6), we impose the boundary conditions on the four boundaries, which are called as inner, outer, upper and lower boundaries. The inner and outer boundaries are defined by the surfaces on which the accelerating electric field is vanishes, that is,  $E_{\parallel} = 0$ . On the inner, upper and lower boundaries, the accelerating potential is equal to zero, that is,  $\Phi = 0$ . On the inner boundary, because both conditions  $E_{\parallel} = 0$  and  $\Phi = 0$  are imposed, we can not know the position of the inner boundary in advance. We solve the position of the inner boundary with the dynamics.

The lower boundary is defined by the last-open field line. For the upper boundary, we define with a magnetic field line. For the outer boundary, we define it with a curve line, which is perpendicular to the magnetic field lines in the magnetic meridian plane. For such a case, the upper part of the our gap extends beyond the light cylinder, if we put the outer boundary of the lower part of the gap close to (but inside ) the light cylinder. The present static Poisson equation of (6) will not give the correct solutions for the electric field outside



the light cylinder. As we will see later (Figure 5), however, most  $\gamma$ -rays are emitted from the lower part of the gap. The spectral features will be less affected by the structure of the upper part of the gap. We expect that the results do not change much between the present approximated and correct treatments. To calculate the spectra, we take into account the emissions inside the light cylinder.

### 3.2 Particle motion

To calculate the synchrotron and curvature radiations, we solve an evolution of the particle's momentum using the electric field distribution in the outer gap obtained by the method described in section 3.1. The equation of motion for momenta of the parallel ( $P_{\parallel}/m_e c = \sqrt{\Gamma^2 - 1} \cos \theta_p$ ) and perpendicular ( $P_{\perp}/m_e c = \sqrt{\Gamma^2 - 1} \sin \theta_p$ ) to the magnetic field lines are, respectively, described as (Harding et al. 2005; Hirotani 2006)

$$\frac{dP_{\parallel}}{dt} = eE_{\parallel} - P_{sc} \cos \theta_p, \quad (8)$$

and

$$\frac{dP_{\perp}}{dt} = -P_{sc} \sin \theta_p + \frac{c}{2B} \frac{dB}{ds} P_{\perp}, \quad (9)$$

where  $\theta_p$  is the pitch angle,  $P_{sc}$  represents the radiation drag of the synchrotron and curvature radiation, and the second term on the right hand side on equation (9) represents the adiabatic change along the dipole field line. The radiation drag,  $P_{sc}$ , of the synchrotron-curvature radiation is described by (Cheng & Zhang 1996),

$$P_{sc} = \frac{e^2 c \Gamma^4 Q_2}{12 r_c} \left( 1 + \frac{7}{r_c^2 Q_2^2} \right), \quad (10)$$

where

$$r_c = \frac{c^2}{(r_B + R_c)(c \cos \theta_p / R_c)^2 + r_B \omega_B^2}, \quad (11)$$

$$Q_2^2 = \frac{1}{r_B} \left( \frac{r_B^2 + R_c r_B - 3 R_c^2}{R_c^3} \cos^4 \theta_p + \frac{3}{R_c} \cos^2 \theta_p + \frac{1}{r_B} \sin^4 \theta_p \right) \quad (12)$$

$$r_B = \frac{\Gamma m_e c^2 \sin \theta_p}{e B}, \quad \omega_B = \frac{e B}{\Gamma m_e c}. \quad (13)$$

### 3.3 Model parameters

The model parameters are the magnetic inclination angle  $\alpha$  and the current components  $(j_1, j_2)$ , where  $j_1$  (or  $j_2$ ) is the current carried by the positrons (or electrons) coming into the gap through the inner (or outer) boundary. We also use the outer boundary as the model

parameter. As the lower boundary of the gap, we define the last-open field line. For the upper boundary of the middle age pulsars, which we discuss in the paper, we use the critical field line defined by equation of (1). Setting the model parameters, we solve the position of the inner boundary, the accelerating electric field, and the current component carried by particles created in the gap.

The created current, and the resultant calculated flux are determined by the value of the injected currents at the inner boundary  $j_1$  and at the outer boundary  $j_2$ . In fact, the magnitude of the created current is less affected by the current  $j_1$  injected at the inner boundary, but is determined by  $j_2$  injected at the outer boundary, because most of pairs are created between the ingoing  $\gamma$ -rays and the outward propagating surface X-rays. In this paper, we choose the value of the component  $j_2$  so that the created pairs produce the comparable  $\gamma$ -ray flux with the observations.

The created current and the  $\gamma$ -ray flux do not monotonically increase with the current component  $j_2$ . This is because an increase of the created current strengthens screening of the accelerating electric field. With a smaller electric field, the  $\gamma$ -ray photons with a lower energy are produced, and therefore a smaller amount of the pairs are created. Namely, the increment of the created current is determined under the competition between the increase of  $j_2$  and the screening of the electric field. For example, if we assume the current  $j_2 = 0.003$  in units of Goldreich-Julian value, we obtain the created current of  $j_g \sim 0.3$  for the Geminga pulsar with  $\alpha = 60^\circ$ . Then if we double the value of  $j_2$ , we find from the numerical results that the increments of the created current and the total luminosity are factors of  $\sim 1.3$  and  $\sim 1.2$ , respectively. We find that the computed  $\gamma$ -ray flux is not sensitive to the detailed values of the current components injected at the boundaries.

Since the magnetic field must be modified by the rotational and the plasma effects the vicinity of the light cylinder (Muslimov & Harding 2005), the last-open field line will be also different from the conventional magnetic surface, which is tangent to the light cylinder for the vacuum case. For example, Romani (1996) assumed the last-open lines with the field lines which have the polar angle  $\theta_{pc} \sim 1.4^{1/2}\theta_{pc,0}$  at the stellar surface, where  $\theta_{pc,0}$  is the conventional polar cap angle (3) for static dipole field. In the studies of the force-free magnetosphere,  $\theta_{pc} \sim 1.36^{1/2}\theta_{pc,0}$  was obtained by Contopoulos et al. (1999) and  $\theta_{pc} \sim 1.27^{1/2}\theta_{pc,0}$  by Gruzinov (2005). In the paper, we use  $\theta_{pc} \sim 1.36^{1/2}\theta_{pc,0}$  for the last-open field lines. The position of the last-open field lines affects the accelerating electric field, spectrum and the pulse profile. For example, if we adopt a vacuum solution, the typical electric field in

the gap is described as  $E_{||} \sim B_* R_*^2 \delta\theta_{gap}^2 / c R_c$  with  $B_*$  begin the stellar magnetic field (Cheng et al. 2000; Hirotani 2006). Then as the last-open field line is located on the magnetic field line with a larger polar angle on the stellar surface, we obtain a stronger accelerating electric field because (i) the trans-field thickness of the gap,  $\delta\theta = \theta_{pc} - \theta_c$ , becomes large and (ii) the typical curvature radius of the magnetic field line, on which most  $\gamma$ -rays are emitted, becomes small. As a result, a spectrum of the radiation from the gap becomes hard. For the pulse profiles, the phase separation between two peaks becomes wide as the last-open field shift to inner magnetosphere from the canonical field line, which is tangent to the light cylinder (Takata & Chang 2007). In fact, the calculated  $\gamma$ -ray spectrum and pulse profiles with the last-open field lines for  $\theta_{pc} \sim 1.36^{1/2} \theta_{pc,0}$  are more consistent with the observations for the Geminga pulsar than those for  $\theta_{pc} \sim \theta_{pc,0}$  (section 5).

#### 4 THREE-DIMENSIONAL GEOMETRICAL MODEL

The observed pulse profile provides an important tool for diagnose the geometry of the emission region in the pulsar magnetospheres. In particular, number of the peaks in a single rotational period, positions of the peaks in the pulse profile, and morphology of the pulse profiles at different energy bands will discriminate the emission models.

In the framework of the outer gap model (and also the slot gap model), the peaks appear in the pulse profiles because the photons emitted various point pileup due to the effect of the special relativity correction; the aberration of the emitting direction and the flight time (Romani & Yadigaroglu 1995; Dyks & Rudak 2003). To compute the pulse profile, we anticipate that the emission direction coincides with the particle motion. In the observer frame, the particle motion along the field lines in the north hemisphere is described by  $\mathbf{v} = \pm v_0 \mathbf{b} + v_{co} \mathbf{e}_\phi$ , where the plus (or minus) sign represents the outgoing (or ingoing) particles,  $v_0$  is the velocity along the magnetic field line and is determined by the condition that  $|\mathbf{v}| = c$ ,  $\mathbf{b}$  is the unit vector of the magnetic field, for which we adopt a rotating dipole field in the observer frame,  $v_{co}$  is the co-rotating velocity, and  $\mathbf{e}_\phi$  is the unit vector of the azimuthal direction. The emission direction,  $\mathbf{n} \equiv \mathbf{v}/c$ , is interpreted in terms of the viewing angle  $\xi = n_z$  and the pulse phase  $\Phi = -\phi_e - \mathbf{n} \cdot \mathbf{r}_e / R_{lc}$ , where  $\phi_e$  and  $r_e$  is the azimuthal emission direction and the radial distance to the emission point, respectively. We use a rotating magnetic dipole field in the observer frame to compute the pulse profile.

The distribution of emissivity affects the pulse profiles. For the distribution of the emis-

sivity in the meridional plane, we use the results of the two-dimensional electrodynamic model, which solves the trans-field distribution of the emissivity in the magnetic meridional plane (see section 5.1.3). For the structure of the azimuthal direction, it is difficult to model without solving a three-dimensional dynamics. For the first order approximation, however, we may apply the function form of the accelerating electric field for the vacuum solution. In the vacuum solution, the typical value of the electric field along a field line is determined by  $E_{||}(\phi) \propto R_n(\phi)^{-1}$  with  $R_n$  being the curvature radius at the null charge surface and  $\phi$  the magnetic azimuthal angle of the magnetic field on the stellar surface measured from the magnetic meridional plane (Cheng et al. 1986a; Cheng et al. 2000). In such a case, the number of the curvature photons emitted per second by a particle and the typical energy of the emitted photons are proportional to  $N_c(\phi) \propto R_n^{-3/4}$  and  $E_\gamma \propto R_n^{-1/4}$ , respectively, if we assume the force balance between the particle acceleration and the radiation drag. For example, we obtain  $R_n \sim 0.24R_{lc}$  for the magnetic meridional plane ( $\phi = 0$ ) and  $R_n \sim 0.72R_{lc}$  for  $\phi = 90^\circ$ , if we use  $\theta_{pc} \sim 1.36^{1/2}\theta_{pc,0}$  for the last-open field lines with the inclination angle  $\alpha = 60^\circ$ . In this paper, therefore, when we compute the pulse profile, we assume that ratio of the photon number emitted on the field lines of  $\phi = 0^\circ$  and of  $\phi = 90^\circ$  is  $[N(90^\circ)/N(0^\circ)] = (0.72/0.24)^{-3/4} \sim 0.42$ . We do not consider the emissions from the magnetic field lines on which the radial distance to the null charge point is larger than  $r = R_{lc}$ .

## 5 RESULTS

### 5.1 The Geminga pulsar

In this section, we apply the model to the Geminga pulsar and constrain the magnetic inclination and viewing angles. First, we will show structure of the outer gap that occupies most of the region between the last-open line and the critical field line (section 5.1.1). Then we will show that the calculated spectra are consistent with the observations from X-ray through  $\gamma$ -ray bands (section 5.1.2). We use the properties of the observed  $\gamma$ -ray pulse profile to constrain the magnetic inclination and viewing angles of the observer (section 5.1.3). For the Geminga pulsar, the observed pulse profile in  $\gamma$ -ray bands shows double peak structure, and the phase separation of the two peaks is about 0.5 phase. Finally, we further constrain the magnetic inclination angle by discussing visibility of the radio beam in section 5.2, in which we will assume that the radio beam from the Geminga pulsar is oriented in a

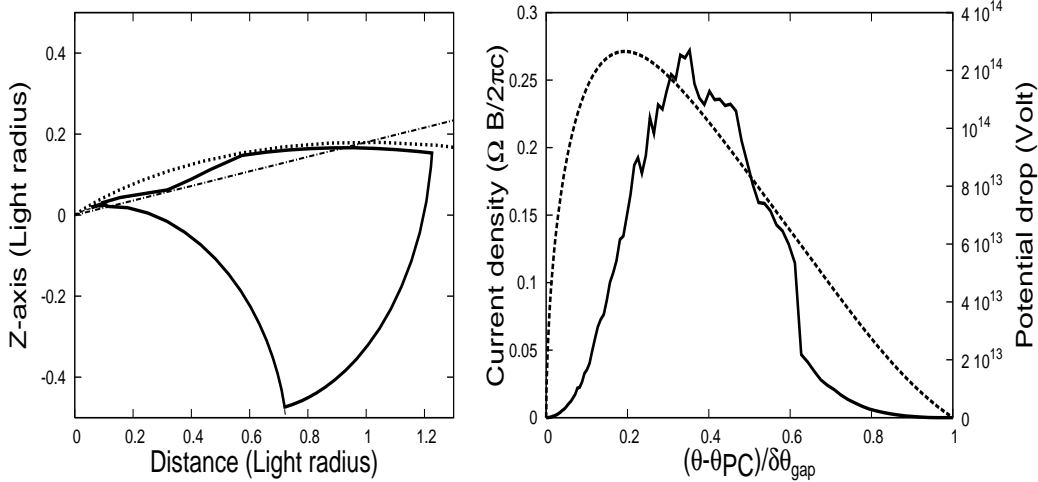


**Figure 2.** Left; The geometry of the outer gap accelerator. The solid line is the boundary of the gap. The dotted lines show the critical line, and the dashed-dotted line is the null surface of the Goldreich-Julian charge density. Right; The trans-field structure of the current (solid) and the electric potential drop (dashed line) along the magnetic field lines as a function of the polar angle of the field lines on the stellar surface. We note that our static approximation will not be good treatment to describe the electric structure beyond the light cylinder. But we expect that the gap thickness and the calculated spectrum will not be affected much the electric structure beyond light cylinder, because most  $\gamma$ -ray photons are radiated from the lower part outer gap inside the light cylinder. The results are for  $\theta_{pc} = 1.36^{1/2}\theta_{pc,0}$ .

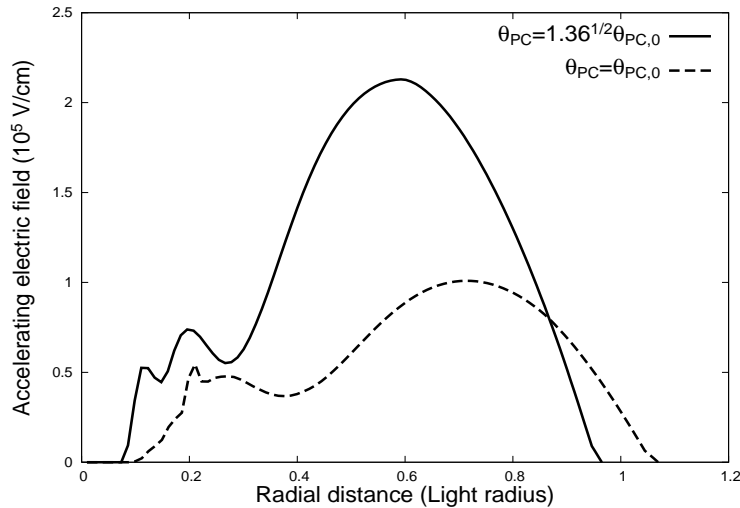


**Figure 3.** The distribution of the accelerating electric field along the magnetic field line, on which the strength of electric field attains the maximum value. The solid and the dashed lines are results from the last-open field lines for  $\theta_{pc} = 1.36^{1/2}\theta_{pc,0}$  and  $\theta_{pc} = \theta_{pc,0}$ , respectively.

different direction from the line of sight. For the Geminga pulsar, we find that the calculated spectrum with the stellar dipole momentum inferred from the rotating dipole model is too soft compared with the observation. For the present calculations, we used double of the dipole momentum inferred from the rotating dipole model.

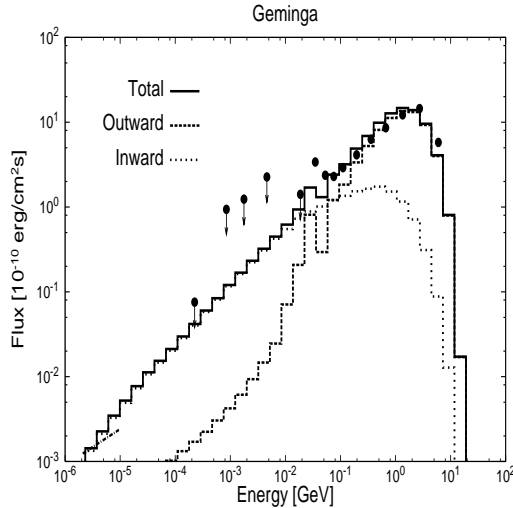
### 5.1.1 Outer gap structure

Figure 2 summarizes the outer gap structure of the Geminga pulsar for the inclination angle that  $\alpha = 60^\circ$ , and for  $j_{1,2} = 3 \cdot 10^{-3}$ , that is 0.3 % of the Goldreich-Julian currents are injected at both inner and outer boundaries. For the last-open field line, we use the magnetic field line that has the polar angle  $\theta_{pc} \sim 1.36^{1/2}\theta_{pc,0}$ , as we discussed in section 3.3

In the left panel in Figure 2, the thick solid line shows the boundary of the obtained gap structure. The dotted and dashed-dotted line represent the critical field line and the null charge surface of the Goldreich-Julian charge density, respectively. As the computed boundary of the gap shows, we can find the solution that the outer gap can occupy whole region between the last-open field line and the critical field line, as we discussed in section 2.

With the right panel of Figure 2, we display the current density carried by the created pairs (solid line) and the total electric potential drop in the gap (dashed line), that is potential drop between the inner and outer boundaries, as a function of the polar angle,  $\theta$ , of the magnetic field lines on the stellar surface. In the abscissa, the polar angle satisfying the condition that  $(\theta_{pc} - \theta)/\delta\theta_{gap} = 0$  is corresponding to the last-open field line, and the angle of  $(\theta_{pc} - \theta)/\delta\theta_{gap} = 1$  is corresponding to the upper boundary of the gap. From the solid line, we can see that the maximum current density of about 30 % of the Goldreich-Julian value runs through along the magnetic field line that penetrates the gap at the height of about 40% of the gap thickness measured from the last-open field line. From the dashed line, we also find that the largest electronic potential drop of  $V \sim 2 \times 10^{14}$  Volt appears on the magnetic field line penetrating the gap at the height of about 20% of the thickness. This indicates that the strength of the accelerating electric field becomes maximum on the magnetic field line penetrating the gap at the height of about 20% of the thickness. Because the emitting power of each magnetic flux tube is proportional to the product of the current density and the potential drop at each field line, we can read that most of emissions come from the height between 20 % and 40 % of the gap thickness (see also Figure 5).

Figure 3 shows the distribution of the electric field along the magnetic field line, on which the strength of the electric field attains the maximum value in the outer gap. We compare the results for  $\theta_{pc} = 1.36^{1/2}\theta_{pc,0}$  (solid line) and  $\theta_{pc} = \theta_{pc,0}$  (dashed line). As the Figure 3 shows, a larger accelerating electric field is obtained if we assume a larger polar cap angle. The typical strength of the accelerating electric field is proportional to  $E_{||} \propto (\delta\theta_{gap})^2/R_c$  (Cheng et al 2000; Hirovani 2006). In the present case, the curvature radius on the field



**Figure 4.** The curvature-synchrotron spectrum for the Geminga pulsar in X-ray and  $\gamma$ -ray bands. The solid line represents the total emissions which includes the outward (dashed line) and the inward (dotted lines) emissions. The filled circles and the dashed-dotted line represent the observed phase-averaged spectrum (after Kargaltsev et al. 2005).

line on which the electric field attains the maximum value is typically  $R_c \sim 0.8R_{lc}$  for  $\theta_{pc} = 1.36^{1/2}\theta_{pc,0}$  and  $R_c \sim 1.2R_{lc}$  for  $\theta_{pc} = \theta_{pc,0}$ . This means that the ratio of strengths of the accelerating electric field for two cases is  $E_{||}|_{\theta_{pc}=1.36^{1/2}\theta_{pc,0}}/E_{||}|_{\theta_{pc}=\theta_{pc,0}} \sim 2$ , which describes the difference of the strengths of the electric field seen in Figure 3. The typical energy of the photons emitted by the curvature radiation is proportional to  $E_c \propto E_{||}^{3/4} R_c^{1/2}$ . The ratio of the typical energies becomes  $E_c|_{\theta_{pc}=1.36^{1/2}\theta_{pc,0}}/E_c|_{\theta_{pc}=\theta_{pc,0}} \sim 1.4$ . As a result, the calculated spectrum for  $\theta_{pc} = 1.36^{1/2}\theta_{pc,0}$  is harder than that for  $\theta_{pc} = \theta_{pc,0}$ .

### 5.1.2 Spectrum

Figure 4 compares the calculated spectrum of the curvature and synchrotron processes with the observations in X-ray through  $\gamma$ -ray bands. The result is for the last-open field lines with the polar angle  $\theta_{pc} = 1.36^{1/2}\theta_{pc,0}$ , and the model parameters are the same with that of Figure 2. In Figure 4, the filled circles and the dashed-dotted line show the observed phase-averaged spectrum. The dashed line and the dotted line represent the emissions of outgoing positrons and of the ingoing electrons, respectively. The solid line represents the total emissions. For each line, the components of the curvature and the synchrotron radiations are combined. In fact, the curvature radiation dominates in the spectrum above 100 MeV, while the synchrotron radiation dominates below 10 MeV. From Figure 4, we see that the total spectrum (solid line) is consistent with the observations in X-ray through  $\gamma$ -ray bands.

If we use the canonical last-open field line with the polar angle  $\theta_{pc} = \theta_{pc,0}$ , the spectral

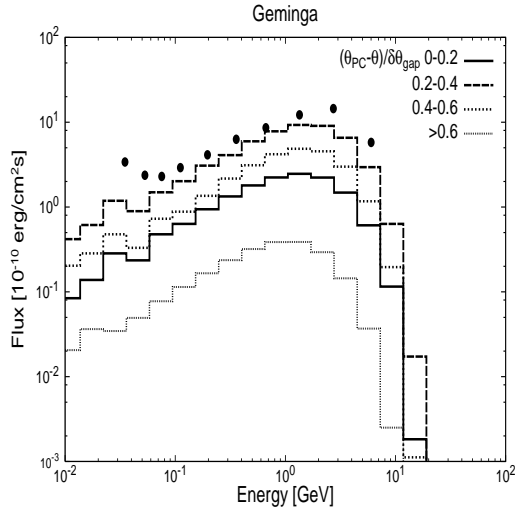


**Figure 5.** The trans-field distribution of the emissivity of the  $\gamma$ -ray emissions. Each line represents the spectrum from the height below 20 % of the thickness measured from the last-open field line, (solid line), between 20 % and 40 % (dashed line), between 40 % and 60 % (dotted line), and above 60 % (dashed-dotted line).

cut off is lactated at the energy factor of  $1/1.4$  smaller than that seen in the solid line of Figure 4, as we discussed in the last paragraph of section 5.1.1. Therefore, the calculated spectrum for the last-open field line with  $\theta_{pc} = 1.36^{1/2}\theta_{pc,0}$  is more consistent with that for the canonical last-open field line.

From Figure 4, we can see that the curvature radiation of outgoing positrons (dashed line) dominate in the total emissions above 100 MeV. This is because most of the pairs are created the vicinity of the inner boundary by the inward propagating  $\gamma$ -rays and the outward propagating surface X-rays. The created electrons and positrons are accelerated inwardly and outwardly by the electric field, respectively. The positrons created around the inner boundary are accelerated by almost whole potential drop in the gap, while the created electrons are accelerated by the potential drop only between the inner boundary and the point where they were created. Therefore, the total radiation power is larger for the outward emissions than the inward emissions. Below 10 MeV, on the other hand, we find that the synchrotron radiation of the ingoing electrons dominate in the calculated spectrum. This is because the synchrotron emissions with strong magnetic field near the stellar surface contribute to the spectrum in X-ray bands.

### 5.1.3 $\gamma$ -ray pulse profiles

We discuss the  $\gamma$ -ray pulse profiles, and constrain the inclination angle and the viewing angle using the three-dimensional geometrical model described in section 4. As Figure 4 shows, the



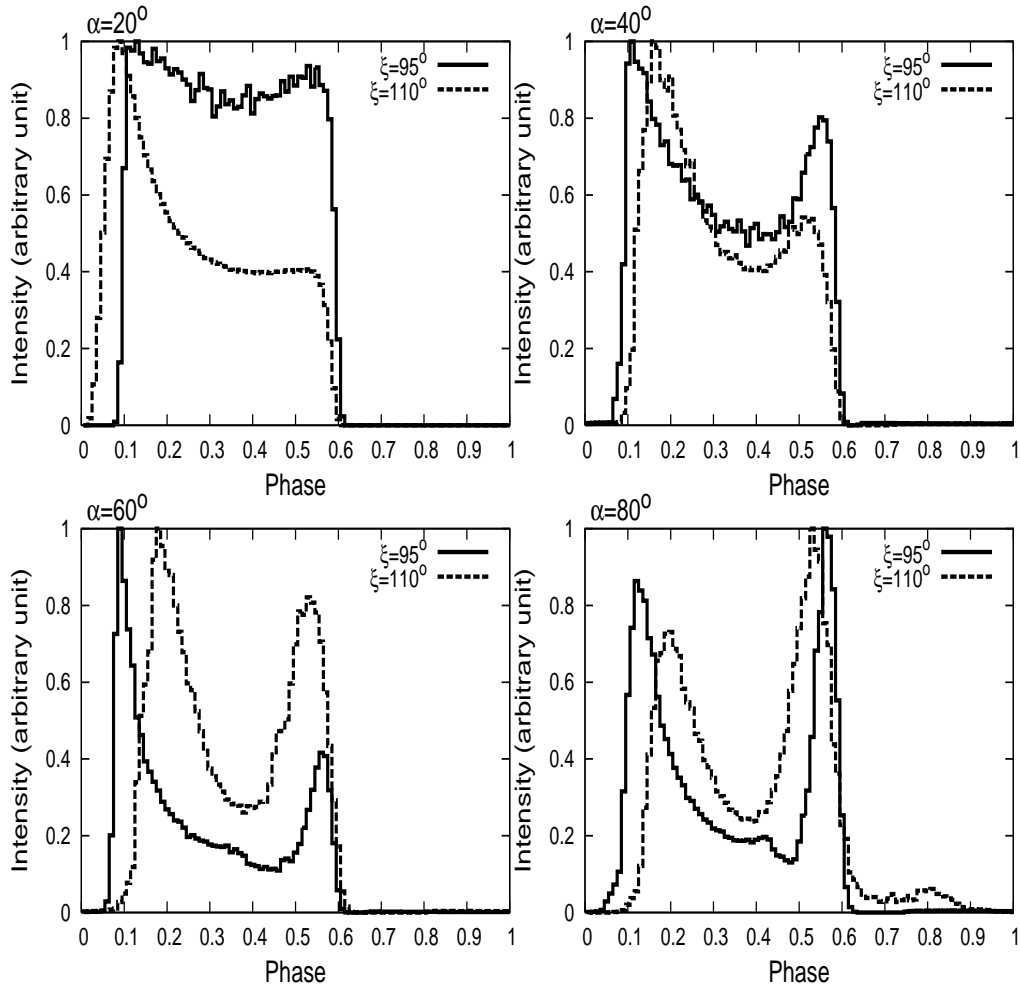


**Figure 6.** Expected pulse profiles in the  $\gamma$ -ray bands for the Geminga pulsar. The upper left, the upper right, the lower left, and the lower right panels show the pulse profiles for the inclination angle of  $\alpha = 20^\circ$ ,  $40^\circ$ ,  $60^\circ$  and  $80^\circ$ . The solid and dashed lines in each pane represent the pulse profiles of the viewing angle  $\xi = 85^\circ$  (or  $95^\circ$ ) and  $70^\circ$  (or  $110^\circ$ ), respectively. The results are for  $\theta_{pc} = 1.36^{1/2}\theta_{pc,0}$ .

outward emissions dominate in the total spectrum above 100 MeV. In this section, therefore, we consider only the outward emissions to compute a pulse profile.

For the trans-field distribution of the emissivity in the poloidal plane, we use the results of the two-dimensional electrodynamic study. In Figure 5, we can read the trans-field distribution of the emissions above 10 MeV bands. For example, the dashed line represents the spectra of the emissions from the height between 20 % and 40 % of the thickness measured from the last-open field line. By comparing the magnitude of the fluxes between the solid and dashed lines in Figure 5, we may put an emissivity at the height below 20% of the gap about one order smaller than that at the height between 20% and 40% of the gap.

Figure 6 summarizes the pulse profiles for the magnetic inclination angle,  $\alpha = 20^\circ$  (upper

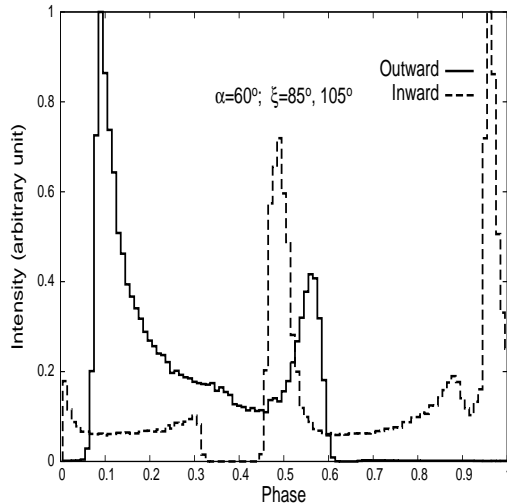


**Figure 7.** The pulse profile of the Geminga pulsar with the inclination angle  $\alpha = 60^\circ$  and the viewing angle  $\xi = 85^\circ$  (or  $105^\circ$ ). The solid and dashed lines represent the pulse profiles for the outward and inward emissions, respectively. Above 100 MeV bands, only outward emissions contribute to the spectrum (Figure 4) so that the pulse profile (solid line) becomes double peak structure. For around 10 MeV bands, both the outward and inward emissions contribute to the pulsar profile, and the pulse profile has the four peaks in a single period. For X-ray bands, the inward emissions dominate in the pulse profile, which has two peaks (dashed line) in a single period.

left panel),  $\alpha = 40^\circ$  (upper right panel),  $\alpha = 60^\circ$  (lower left panel) and  $\alpha = 80^\circ$  (lower right panel). We calculate the emissions from the whole region between the last-open field lines and the critical field lines. The results are for the last-open field lines with the polar angle  $\theta_{pc} = 1.36^{1/2}\theta_{pc}$ . If we used the canonical last-open field lines with  $\theta_{pc} = \theta_{pc}$  to computed pulse profile, we found that no geometries (inclination angle and viewing angle) can produce the observed phase separation between the two peaks with the  $\gamma$ -ray spectrum; we obtained narrower phase separation ( $\delta\phi < 0.4$ ) than the observation  $\delta\phi \sim 0.5$ .

In Figure 6, the solid and dashed lines are results for the viewing angle of  $\xi = 85^\circ$  (or  $95^\circ$ ) and  $\xi = 70^\circ$  (or  $\xi = 110^\circ$ ). As the same with the conventional outer gap model, the first peak in the pulse profile is made by the emissions from leading part of the gap according to the rotational direction, while the second peak is made by the emissions from trailing part of the gap. We can see from Figure 6 that the morphology of the pulse profiles depends on the inclination and viewing angles. By comparing the observed pulse profile, therefore, we can constrain the inclination and viewing angles. First we can rule out nearly aligned rotator, as represented by the pulse profile for  $\alpha = 20^\circ$ . With such a small inclination angle, a sharp second peak does not appear in the pulse profile for any viewing angles of the observer. Secondary, we would rule out the viewing angle far away from  $\xi = 90^\circ$  as demonstrated by the pulse profile (dashed line) with  $\xi = 70^\circ$  in Figure 6. In such a viewing angle, the pulse profile has a single broad peak or the two peaks with a narrower separation of the phases

compared with the observations ( $\sim 0.5$  phase). Therefore, a larger inclination angle and the viewing angle that  $\xi \sim 90^\circ$ , say  $80^\circ < \xi < 100^\circ$ , are preferred to explain the observed pulse profile of  $\gamma$ -ray bands.

#### 5.1.4 Pulse profiles below 10 MeV

In this section, we discuss the expected pulse profile in soft  $\gamma$ -ray and the X-ray bands. As the calculated spectrum in Figure 4 shows, the inward emissions from the inward particles contribute to the total spectrum below 10 MeV. Specifically, both the inward and the outward emissions contribute to the total emissions around 10 MeV, while the only inward emissions dominate into the total emission in X-ray bands. Therefore, we expect that the pulse profile below 10 MeV is not simply an extension of that of the  $\gamma$ -ray bands above 100 MeV. Figure 7 shows the pulse profile for the outward (solid) and the inward (dashed) emissions for  $\alpha = 60^\circ$  and  $\xi = 85^\circ$  (or  $95^\circ$ ). From the dashed line in Figure 7, we find that the pulse profile of the inward emissions has also double peak structure. For the inward emissions, the first peak is made by the emissions from the trailing part of the gap and the second peak is made by the emissions of the leading part of the gap.

For the calculated spectrum around 10 MeV in Figure 4, both the outward and inward emissions contribute to the spectrum. The pulse profiles in 10 MeV bands will be made by both the outward (solid line in Figure 7) and inward (dashed line in Figure 7) emissions. Therefore, we expect that the pulse profile in soft  $\gamma$ -ray bands will have four peaks in a single period.

In X-ray bands, the inward emissions dominate in the total emissions (Figure 4). Therefore we expect the double peak structure of the pulse profile in the X-ray bands for the Geminga pulsar. By comparing between the predicted pulse profiles in  $\gamma$ -ray (solid line) above 10 MeV bands and X-ray bands (dashed line), the pulse peaks in X-ray band will appear in the leading phases of the pulses of the  $\gamma$ -ray bands.

With the present results, the observed differences of the pulse morphologies in the different wavelength are strong tool to diagnose the emission processes in the pulsar magnetosphere. For the Vela pulsar, the outer gap model can explain the morphology differences between the pulse profiles in RXTE and EGRET bands (Takata et al. 2008). For the Geminga pulsar, the spectrum and the pulse profiles observed by *ROAST* and *ASCA* indicated that the non-thermal X-rays and  $\gamma$ -rays are produced by a distinct mechanism

(Jackson et al. 2002). Kargaltsev et al. (2005) analyzed X-ray spectrum and pulsations observed by *XMM – Newton*. They found that the pulse profile of the non-thermal X-rays in 2-8 keV bands has two peaks in a single period, and that the spectrum and pulse profile are not simply an extension of that of the EGRET bands. The observed pulse morphologies for the Geminga pulsars are different in the different wave length. As we discussed above, the present model also predicts the double peak structure in X-ray pulse profile and the energy dependent pulse profiles from X-ray through  $\gamma$ -ray bands. The results of the present model are generally consistent with the observed pulse profiles in X-ray and  $\gamma$ -ray bands. For the phase separation between two peaks in X-ray bands, however, the observations in 2-8 keV bands imply about 0.35 (0.65) phase (Kargaltsev et al. 2005), while the present model predicts about 0.5 phase (dashed line in Figure 7). So, it may be required an examination of the X-ray pulse profile with a more realistic magnetic field configuration.

## 5.2 Radio “quiet” observations

The Geminga pulsar is the only known radio quiet (or weak emissions)  $\gamma$ -ray pulsar. Based on the following reasons, we assume that the radio beam of the Geminga pulsar is oriented in a different direction from the line of sight. First, there are many radio pulsars around the Geminga pulsar on  $P - \dot{P}$  diagram. Second, Lin & Chang (2008) searched candidate periods in unidentified EGRET sources for the next Geminga. They found that most of the candidate timing properties belong to that of Vela-like pulsars. If their candidate periods are true, their results would suggest that the major cause for a radio quiet is likely geometrical rather than intrinsic.

The radio emission model with the assumption that the radio “quiet” for the Geminga pulsar is caused by geometry also provides a tool to study the magnetic inclination angle and the viewing angle with the  $\gamma$ -ray emission model. For the emission height of the outer cone of the radio emissions, we apply the empirical model developed by Kijak & Gil (2003). They found a relation among the emission height, the rotation period, the period time derivative and the frequency of the radio wave. Assuming the rim of the radio beam are emitted vicinity of the critical magnetic field line (defined by  $\theta_c$ ), their relation is described as

$$r \sim 40R_*(\theta_{PC}/\theta_c)^2 P^{0.3} (\dot{P}/10^{-15} \text{ss}^{-1})^{0.07} \nu_{\text{GHz}}^{-0.26}, \quad (14)$$

where  $R_*$  is the stellar radius and  $\nu$  is the frequency of the radio wave.

Figure 8 shows photon mapping of the rim of the radio beam emitted at the height

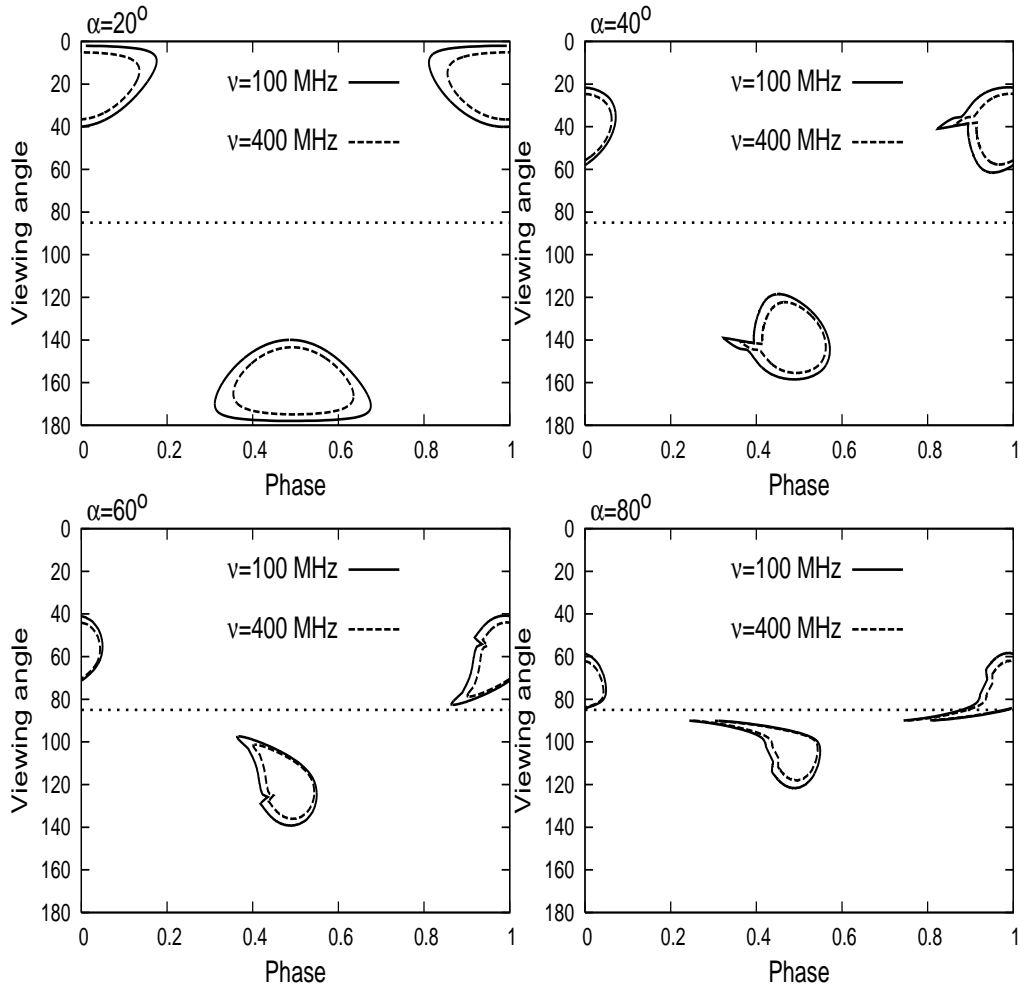


**Figure 8.** Photon mapping of the outer rim of the radio beam emitted at the height described by equation of (14) for different inclination angles  $\alpha = 20^\circ$  (upper left),  $40^\circ$  (upper right),  $60^\circ$  (lower left) and  $80^\circ$  (lower right). The dotted line represent viewing angle of  $\alpha = 85^\circ$ .

described by equation of (14) for different inclination angles. We used the rotating dipole field as the magnetic field of the magnetosphere. In Figure 8, the solid and dashed lines represent the emissions for the frequencies of  $\nu = 100$  MHz and 400 MHz, respectively. For the references the dotted line represents line of sight for the viewing angle of  $\xi = 85^\circ$ .

For a small inclination angle represented by  $\alpha = 20^\circ$  (upper left panel in Figure 8), an observer with  $\xi \sim 90^\circ$ , which is preferred to explain observed  $\gamma$ -ray pulse profile, does not measure the radio emission. This is because the magnetic pole points in a completely different direction from the line of sight for  $\xi \sim 90^\circ$ . For largely inclined pulsar such as  $\alpha = 80^\circ$  (lower right panel), on the other hand, it is highly possible to be measured the radio emissions by the observer with  $\xi \sim 90^\circ$ , because the magnetic pole points close to the

Pulsar	$P$ (s)	$\dot{P}$ ( $10^{-13}$ s/s)	$B$ ( $10^{-12}$ G)	$\tau$ ( $10^5$ yr)	$d$ (kpc)	$\dot{E}/d^2$ $10^{-10}$ erg/cm <sup>2</sup> s	$\alpha$	$\xi$	Fermi
Geminga	0.2371	0.1097	1.63	3.42	0.16	1300	$\sim 50^\circ$	$\sim 90^\circ$	O
B0355+54	0.1564	0.04397	0.839	5.64	1.10	38.9	$51^\circ$	$55^\circ$	O
B0740-28	0.1668	0.1682	1.69	1.57	1.89	41.0	$37^\circ$	$27^\circ$	×
B1449-64	0.1795	0.02746	0.71	10.4	1.84	5.88	$55^\circ$	$63^\circ$	O
B1929+10	0.2265	0.01157	0.518	31	0.36	31.5	$35^\circ$	$60^\circ$	O

**Table 1.** Timing properties of the middle-aged pulsars.  $P$  is the rotational period,  $\dot{P}$  is the time derivative of the rotational period,  $B$  is the stellar magnetic field inferred from the dipole field model,  $\tau$  is the pulse age,  $d$  is the distance,  $\dot{E}/d^2$  is the spin-down luminosity measured on Earth,  $\alpha$  is the magnetic inclination angle, and  $\xi$  is the viewing angle. For the magnetic inclination angle  $\alpha$  and the viewing angle  $\xi$ , we refer the present paper for the Geminga pulsar, Rankin (1993) for PSRs B0355+54, B0740-28 and B1449-64, and Everett and Weisberg (2001) for PSR B1929+10. In the last column, we show the predicted detectability of pulsed  $\gamma$ -ray emissions by Fermi telescope with  $5\sigma$  in 50 hours.

line of sight. For the Geminga pulsar, therefore, a smaller inclination angle is preferred to explain the radio “quiet” observations with the  $\gamma$ -ray detections.

Using the observed pulse profiles in the  $\gamma$ -ray observations discussed in section 5.1.3, we safely eliminated the possibility of the nearly aligned rotator such as  $\alpha = 20^\circ$  because predicted single peak structure (upper left panel in Figure 6) is not consistent with the observed double peak structure of the  $\gamma$ -ray pulse. Combing those results obtained by analysis in the  $\gamma$ -ray and the radio “quiet” observations, we conclude that the Geminga pulsar has a moderate magnetic inclination angle of  $\alpha \sim 50^\circ$ , and we observe the Geminga pulsar with a viewing angle of  $\xi \sim 90^\circ$ .

### 5.3 Another middle-aged pulsars

We apply the present outer gap model to another middle-aged pulsars. Using ATNF Pulsar Catalogue (Manchester et al. 2005, see <http://www.atnf.csiro.au/research/pulsar/psrcat>), we chose four middle-aged pulsars, PSRs B0355+54, B0740-28, B1449-64, and B1929+10, to discuss the detectability of the  $\gamma$ -ray emissions from the outer gap by Fermi telescope. These four pulsars were chosen with the following conditions. If the pulsars are at a large distance from the Earth, Fermi telescope could not measure the  $\gamma$ -ray emissions from the pulsars. A rough idea of the  $\gamma$ -ray flux on the Earth is described by  $\eta L_{sp}/d^2$ , where  $\eta$  is efficiency,  $L_{sp}$  is the spin-down luminosity, and  $d$  is the distance to the pulsar. Our four pulsars have the spin-down luminosity so that  $\eta L_{sp}/d^2$  with  $\eta = 0.01$  of the Geminga pulsar is larger than  $10^{-12}$  erg/cm<sup>2</sup>s, which is close to the lower limit of Fermi telescope detection with  $5\sigma$  in 50 hours.

Second, there is the possibility that we can not measure the  $\gamma$ -ray emissions, because the

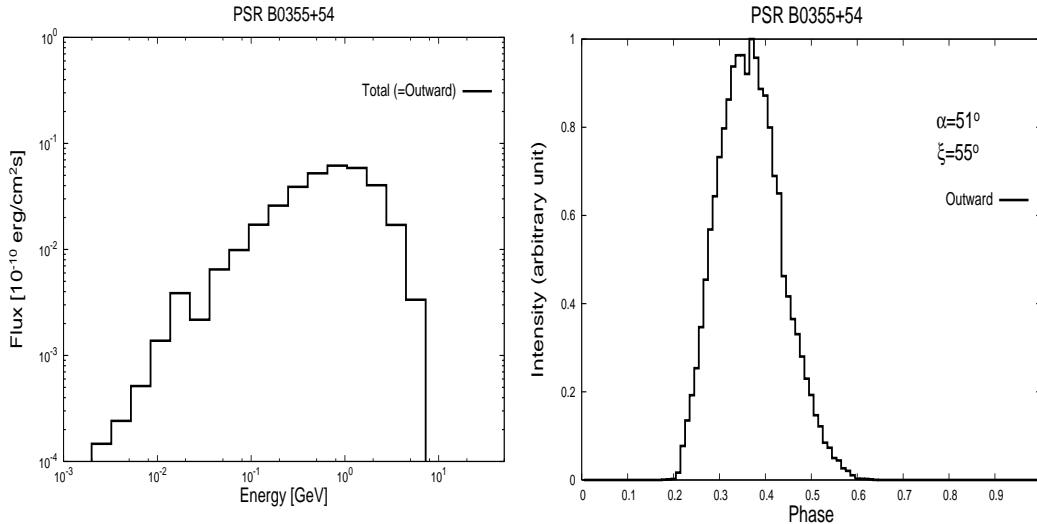


**Figure 9.** The  $\gamma$ -ray spectrum (left) and pulse profile (right) for PSR B0355+54. For  $\alpha = 51^\circ$ , the observe with  $\xi \sim 55^\circ$  measures only the outward emissions.

$\gamma$ -ray beam is oriented in a different direction from the line of sight. Because the geometry of the  $\gamma$ -ray beams depends on the emission models, the detectability of the  $\gamma$ -ray emissions depends on the models. If we know the viewing angle and the magnetic inclination angle of the pulsar, we can test the models with Fermi observations. On these ground, we chose those four pulsars because the magnetic inclination and viewing angles are inferred from the radio polarization data (Rankin 1993; Everett & Weisberg 2001). In Table 1, we summarize the timing properties of the four pulsars and the Geminga pulsar. The represented results in this section were computed with (i) the double of the dipole inferred from the rotating dipole model and with (ii) the last-open field lines with the polar angle  $\theta_{pc} = 1.36^{1/2}\theta_{pc,0}$ .

### 5.3.1 PSR B0355+54

PSR B0355+54 has a rotational period of  $P = 0.1564$  s (Manchester et al. 1972), which is the fastest in the four pulsars we chose. The distance from the Earth is  $d \sim 1.1$  kpc (Hobbs et al. 2004). PSR B0355+54 is known to emit the X-ray (McGowan et al. 2006) and probably TeV  $\gamma$ -rays (Senecha et al. 1995) from its pulsar wind nebula. The polarization data on the radio wave can be fitted by the rotational vector model; the magnetic inclination and the viewing angles are inferred as  $\alpha \sim 51^\circ$  and  $\xi \sim 55^\circ$ , respectively (Rankin 1993).

Figure 9 shows the expected spectrum (left panel) and the pulse profile (right panel) in  $\gamma$ -ray bands for PSR B0355+54. For the current components injected at the inner and outer boundaries, we used  $j_1 = j_2 \sim 0.01$ . For the inclination angle  $\alpha = 51^\circ$ , the observer with the viewing angle  $\xi = 55^\circ$  can not measure the inward emissions from the outer gap. The model

predicts the emission flux around 1 GeV are about  $F \sim 10^{-11}$  erg/s, which will be able to be measured by Fermi telescope. With the viewing angle  $\xi \sim 55^\circ$ , the expected pulse profile has a broad peak in a single rotational period, as right panel in Figure 9 shows.

### 5.3.2 PSR B0740-28

PSR B0740-28 is younger and faster rotating pulsar than the Geminga pulsar (Bonsignori-Facondi et al 1973). The distance to the pulsar is  $d = 1.89$  kpc (Hobbs et al. 2004) and the magnitude of  $L_{sp}/d^2$  is the largest in the four pulsars. The pulsar wind powered by PSR B0740-28 was discovered in optical bands (Jones et al. 2002). The magnetic inclination angle  $\alpha \sim 37^\circ$  and the viewing angle  $\xi \sim 27^\circ$  are inferred with the polarization characteristics of the radio wave (Rankin 1993).

We will not expect the detection of the  $\gamma$ -ray beam by Fermi telescope from PSR B0740-28, because the  $\gamma$ -ray beam will be oriented in a different direction from the line of sight. Because the viewing angle with  $\xi \sim 27^\circ$  points between the rotational and magnetic axes in the magnetic meridional plane, the observer measures mainly emissions inside the null charge surface and on the magnetic field lines toward rotational axis. However, the outer gap does not predict a strong emissions from that region, but predicts a strong emission beyond the null charge surface and on the magnetic field lines curved away from the rotational axis. The present outer gap model expects that the strong emissions from the outer gap of PSR B0740-28 is oriented in a different direction from the line of sight.

For the slot gap model (Harding et al. 2008), on the other hand, a detection of  $\gamma$ -ray emissions from PSR B0740-28 may be expected, because the model assumes the emissions from the polar cap region to the vicinity of the light cylinder above the whole last-open field lines (Dyks & Rudak 2003). Therefore, PSR B0740-28 will be a good candidate to discriminate the outer gap model and the slot-gap model with Fermi telescope.

### 5.3.3 PSR B1449-64

PSR B1449-64 has the rotational period  $P = 0.1785$  and the period time derivative  $\dot{P} = 2.746 \cdot 10^{-15}$  s/s (Large et al. 1969). The distance to the pulsar is  $d = 1.84$  kpc (Siegman et al. 1993). The magnetic inclination of  $\alpha \sim 56^\circ$  and the viewing angles of  $\xi \sim 63^\circ$  are used to fit the polarization data of the radio wave with the rotating vector model (Rankin 1993). Figure 10 shows the expected spectrum (left panel) and the pulse profile (right panel) in



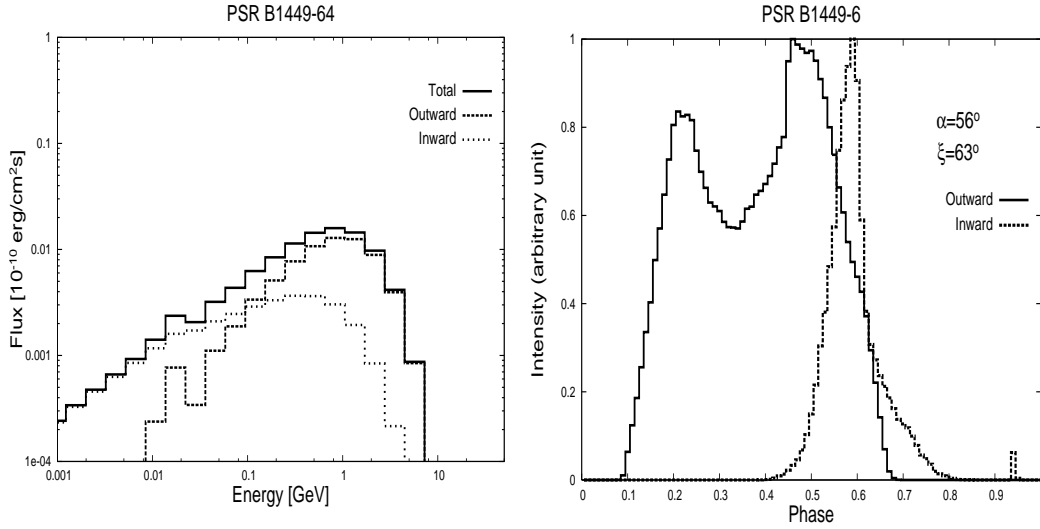


**Figure 10.** The  $\gamma$ -ray spectrum (left) and pulse profile (right) for PSR B1449-64. In the left panel, the solid, dashed and dotted lines represent the spectra of the total, outward and inward emissions. In the right panel, the solid and dashed show the pulse profile of the outward and inward emissions, respectively.

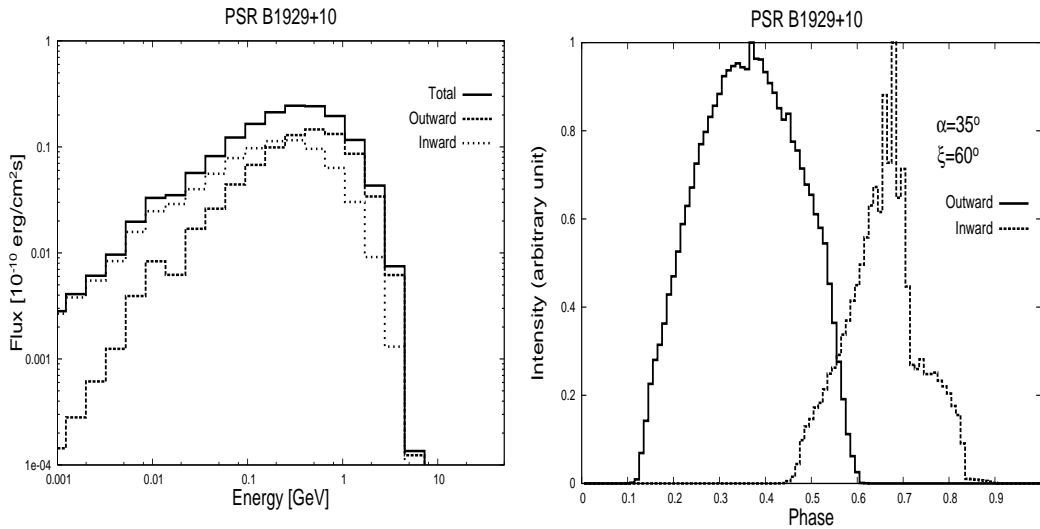


**Figure 11.** The  $\gamma$ -ray spectrum (left) and pulse profile (right) for PSR B1929+10. The lines correspond to same case as Figure 10.

$\gamma$ -ray bands for PSR B1449-64. The expected pulse profile shows the double peak structure. We adopt  $j_1 = j_2 = 0.02$  for the current components injected at the inner and the outer boundaries.

#### 5.3.4 PSR B1929+10

PSR B1929+10 is known as one of the closet pulsar with the distance  $d \sim 0.36$  kpc (Hobbs et al. 2004). PSR B1929+10 is the oldest pulsar  $\tau \sim 3 \cdot 10^6$  yrs in the pulsars we chose with its rotation period  $P = 0.2265$  s and the period time derivative  $\dot{P} = 1.157 \cdot 10^{-15}$  s/s. The

X-ray emissions from both the pulsar and the pulsar wind nebula have been reported (Becker et al. 2006; Hui and Becker 2008). The inferred magnetic inclination and the viewing angle of the observer from the radio polarization are  $\alpha \sim 35^\circ$  and  $\xi \sim 60^\circ$ , respectively (Everett and Weisberg 2001). We use  $j_1 = j_2 = 0.1$  for the currents injected the inner and outer boundaries.

Because of the closeness to the Earth of PSR B1920+10, the expect  $\gamma$ -ray flux can significantly exceed the lower limit of Fermi telescope detection with  $5\sigma$  in 50 hours (Figure 11), although the spin-down power and therefore the  $\gamma$ -ray luminosity are the smallest in the four pulsars. For the pulse profile, we expect single peak in a single rotation period.

## 6 SUMMARY

We summarize the results of our work as follows.

1. We have studied the non-thermal emissions of the Geminga pulsar with the outer gap accelerator model. We solved the accelerating electric field with the pair creation and the radiation processes in the magnetic meridional plane. We demonstrated that the calculated spectrum of the curvature and the synchrotron emissions is consistent with the observation in X-ray through  $\gamma$ -ray bands. The outward curvature radiation dominates in the spectrum of  $\gamma$ -ray bands, while the inward synchrotron emissions dominate in X-ray bands.

2. We demonstrated that the  $\gamma$ -ray pulse above 100 MeV has two peaks, which are made by the outward emissions. Around 10 MeV bands, we expect four peaks in a single period with both the outward and inward emissions. In X-ray bands, the pulse profile has two peaks made by the inward emissions. The pulse phase in X-ray bands are not in phase with that in the  $\gamma$ -ray bands. The model predicts the energy dependent pulse morphology in X-ray through  $\gamma$ -ray bands, which is also indicated by the observations. (Jackson et al. 2002; Kargaltsev et al. 2005).

3. We discussed the inclination angle and the viewing angle for the Geminga pulsar with the pulse morphology. The observed double peak structure in EGRET bands rules out nearly aligned rotator. Assuming that the radio beam from the Geminga pulsar is oriented in a different direction from the line of sight, a greatly inclined magnetic axis is also ruled out. The observed phase separation of two peaks in  $\gamma$ -ray pulse profiles is explained by a viewing angle  $\xi \sim 90^\circ$ . We conclude that the Geminga pulsar has a inclination angle that  $\alpha \sim 50^\circ$  and a viewing angle that  $\xi \sim 90^\circ$ .

4. We applied our method to another four middle-aged radio pulsars, whose spin-down power and distant from the Earth expect the potential of the detection of the  $\gamma$ -ray emissions from those pulsars by Fermi telescope. Applying the inclination angle and the viewing angle inferred from the radio polarization characteristics, we discussed the visibility of the  $\gamma$ -ray emissions from the outer gap. We predict that  $\gamma$ -ray emissions from PSRs B0355+54, B1449-64 and B1929+10 are detectable by Fermi telescope. For PSR B0740-28, the  $\gamma$ -ray beam from the outer gap will be oriented in a different direction from the viewing angle. The observations of the PSR B0740-28 by Fermi telescope will probably be useful for studying the emission site of not only the  $\gamma$ -rays but also the radio wave in the pulsar magnetospheres.

## ACKNOWLEDGMENTS

The authors appreciate fruitful discussion with K.S. Cheng, K.Hirotsu, K.S. Cheng, S. Shibata, and R.Taam. Authors also thank anonymous referee for his/her insightful comments on the manuscript. This work was supported by the Theoretical Institute for Advanced Research in Astrophysics (TIARA) operated under Academia Sinica and National Science Council Excellence Projects program in Taiwan administered through grant number NSC 96-2752-M-007-002-PAE.

## REFERENCES

- Arons J., 1983, ApJ, 266, 215  
Becker W., et al., 2006, ApJ, 645, 1421  
Bonsignori-Facondi S.R., Salter C.J. & Sutton J.M., 1973, A&A, 27, 67  
Chang H.-K., Boggs S., Chang Y.-H. for the NCT collaboration, 2007, AdSpR, 40, 1281  
Cheng K.S., Ho C. & Ruderman M. 1986a, ApJ, 300, 500  
Cheng K.S., Ho C. & Ruderman M. 1986b, ApJ, 300, 522  
Cheng K.S., & Zhang L. 1996, ApJ, 463, 271  
Cheng K.S., Ruderman M. & Zhang L. 2000, ApJ, 537, 964  
Contopoulos I., Kazanas D. & Fendt C. 1999, ApJ, 511, 351  
Daugherty J.K. & Harding, A.K., 1996, ApJ, 458, 278  
Dean et al., 2008, Sci, 321, 1183  
Dyks J. & Rudak B., 2003, ApJ, 598, 1201  
Dyks J., Rudak B. & Harding A.K., 2004, ApJ, 607, 939

- Everett J.E. & Weisberg J.M., 2001, *ApJ*, 553, 341
- Fierro J.M., Michelson P.F., Nolan P.L. & Thompson D.J., 1998, *ApJ*, 494, 734
- Grizov A., 2005, *Phys. Rev. Lett.* 94, 021101
- Harding A.K., Stern J.V., Dyks J. & Frackowiak M., 2008, *ApJ*, 680, 1378
- Harding A.K., Strickman M.S., Gwinn C, Dodson R., Moffet D. & McCulloch P., 2002, *ApJ*, 576, 376
- Harding A.K., Usov V.V., Muslimov A.G., 2005, *ApJ*, 622, 531
- Hirotsu K., 2006, *ApJ*, 652, 1475
- Hirotsu K., 2007, *ApJ*, 662, 1173
- Hobbs G., Lyne A.G., Kramer M., Martin C.E. & Jordan C., 2004, *MNRAS*, 353, 1311
- Hui C.Y. & Becker W., 2008, *A&A*, 486, 485
- Jackson M.S., Halpern J.P., Gotthelf E.V. & Mattox J.R., 2002, *ApJ*, 578, 935
- Jones D.H., Stappers B.W. & Gaensler B.M., 2002, *A&A*, 389L, 1
- Kanbach G., Słowikoska A., Kellner S. & Steinle H., 2005, 2005, in Bulik T., Rudak B., Madejski G., eds, *AIP Conf. Proc. Vol. 801, Astrophysical Sources of High Energy Particles and Radiation*. American Institute of Physics, New York, p. 306 Proceeding, 801, 306
- Kargaltsev O.Y., Pavlov G.G., Zavlin V.E. & Romani R.W., 2005, *ApJ*, 625, 307
- Kataoka J., et al., 2005, *Proc. SPIE*, 5898, 133
- Kijak J. & Gil J. 2003, *A&A*, 397, 969
- Large M.I., Vaughan A.E. & Wielebinski R., 1969, *Natur*, 223, 1249
- Lin L.C.-C. & Chang H.-K., 2008, *MNRAS*, 387, 729
- Manchester R.N., Hobbs G.B., Teoh A., Hobbs M., 2005, *AJ*, 129, 1993
- Manchester R.N., Taylor J.H. & Huguenin G.R., 1972, *Nat.*, 240, 74
- McGowan K.E., Vestrand W.T., Kennea J.A., Zane S., Cropper M. & Córdova F.A., 2006, *ApJ*, 647, 1300
- Mestel L., 1999, *Stellar Magnetism*, International Series of Monographs of
- Muslimov A.G. & Harding A.K. 2003, *ApJ*, 588, 430
- Muslimov A.G. & Harding A.K. 2004, *ApJ*, 606, 1143
- Muslimov A.G. & Harding A.K. 2005, *ApJ*, 630, 454
- Rankin J.M., 1993, *ApJS*, 84, 145
- Romani R.W. & Yadigaroglu I.-A. 1995, *ApJ*, 438, 314
- Romani R.W. 1996, *ApJ*, 470, 469
- Ruderman M.A. & Sutherland P.G., 1975, *ApJ*, 196, 51

- Senecha V.K., Bhat C.L., Rawat H.S., Rannot R.C., Sapru M.L., Kaul R.K. & Tickoo A.K., 1995, *A&A*, 302, 133
- Shibata S., 1995, *MNRAS*, 276, 537
- Siegman B.C., Manchester R.N. & Durdin J.M., 1993, *MNRAS*, 262, 449
- Tang P.S. Anisia, Takata J., Jia, J.J., Cheng K.S., 2008, *ApJ*, 676, 562
- Takata J., Shibata S. & Hirotani K. 2004, *MNRAS*, 354, 1120
- Takata J., Shibata S., Hirotani K. & Chang H.-K. 2006, *MNRAS*, 366, 1310
- Takata J. & Chang H.-K., 2007 *ApJ*, 670, 677
- Takata J., Chang H.-K. & Cheng K.S., 2007 *ApJ*, 656, 1044
- Takata J., Chang H.-K. & Shibata S., 2008, *MNRAS*, 386, 748
- Thompson D.J., 2004, in Cheng K.S., Romero G.E., eds, *Cosmic Gamma Ray Sources*. Dordrecht, Kluwer, p. 149
- Vats H.O., Singal A. K., Deshpande M.R., Iyer K.N., Oza R., Shah C.R. & Doshi S., 1999, *MNRAS*, 302, L65